Chemical Engineering Journal 440 (2022) 135910

Contents lists available at ScienceDirect

Chemical Engineering Journal

journal homepage: www.elsevier.com/locate/cej

Shell inspired heterogeneous membrane with smaller bandgap toward sunlight-activated sustainable water purification

Yangyang Feng [a], Chunjia Luo [a], Xushuai Chen [a], Jincui Gu [b,c,*], Yanmei Zhang [a], Min Chao [a], Mengru Li [a], Tao Chen [a,b,c,*], Xi Chen [a], Xun Wang [d,*], Luke Yan [a,*]

[a] Polymer Materials & Engineering Department, School of Materials Science & Engineering, Chang'an University, Xi'an 710064, PR China
[b] Key Laboratory of Marine Materials and Related Technologies, Zhejiang Key Laboratory of Marine Materials and Protective Technologies, Ningbo Institute of Material Technology and Engineering, Chinese Academy of Science, Ningbo 315201, PR China
[c] School of Chemical Sciences, University of Chinese Academy of Science, Beijing 100049, PR China
[d] Key Lab of Organic Optoelectronics and Molecular Engineering, Department of Chemistry, Tsinghua University, Beijing 100084, PR China

ARTICLE INFO

Keywords:
MXene heterojunction
g-C_3N_4
Bandgap
Self-cleaning
Water purification

ABSTRACT

MXene attracts extensive interest due to its unique physicochemical properties and adjustable transmission channels. However, severe membrane fouling has made the separation performance below the theoretical prediction. Introducing solar energy into membrane filtration is fascinating to address this issue. Inspired by nature, here, we constructed an advanced 0D/2D/2D MXene-based heterogeneous layered membrane by coupling the graphitic carbon nitride (g-C_3N_4) and $Ti_3C_2T_x$ (MXene) nanosheets. The titanium dioxide nanoparticles (TiO_2 NPs) and oxygen vacancies were in-situ generated due to the thermodynamical metastability of the $Ti_3C_2T_x$ nanosheets. The produced TiO_2 NPs can broaden the transmission channel and endow this membrane with anti-fouling capacity. Meanwhile, the oxygen vacancy can capture the photogenerated electron and promote effective electron-hole pairs separation. The 0D/2D/2D heterojunction presented a broader light-absorption capacity. Notably, the designed membrane endowed a smaller bandgap (~2.27 eV), which was lower than most previous reports. These features granted it superior self-cleaning ability. Hence, it kept its excellent separation and catalytic degradation capacity with flux recovery ratio greater than 98% after cyclic experiment. The remarkable self-cleaning capability of this membrane manifests its attractive potential application in low-energy and sustainable water purification.

1. Introduction

The freshwater shortage has exerted severe challenges to modern societies.[1] Membrane separation technology is viewed as a promising solution to get clean water.[2] Mainly, two-dimensional (2D) separation membranes have presented great potential for water purification. To date, numerous 2D membranes have been fabricated, such as MXene[3], boron nitride (BN)[4], graphene oxide (GO)[5], graphite phase carbon nitride (g-C_3N_4)[6], covalent organic frameworks (COF)[7], molybdenum disulfide (MoS_2)[8], metal–organic framework (MOF) nanosheets [9], and so forth. Generally, these 2D membranes have ultrathin parallel-stacked structures, and numerous nanochannels were produced among these nanosheets, which serve as the screening channel for ultimate separation efficiency.

$Ti_3C_2T_x$ (MXene), as a fast-growing 2D material, has received comprehensive attention to building advanced separation membranes, benefiting from its rich surface chemistry and unique physicochemical property.[10–11] For one thing, abundant functional components, for example, hydroxyl and terminal oxygen groups, can be introduced onto the surface of the MXene during the etching process. These functional groups can enhance hydrophilicity and provide a reaction platform for secondary functionalization.[10–11] For another, the MXene-based membranes have controllable transmission channels to achieve on-demand separation.[12–13] Until now, the research on MXene-based separation membranes has brought inspiring achievements. However, these membranes are highly susceptible to irreversible membrane fouling because of the severe interfacial adsorption or deposition of contaminations.[14] Similarly, their separation flux decreases with prolonged arising from high mass transfer resistance. Hence, it remains a critical issue to construct MXene-based membranes with self-cleaning

* Corresponding authors.
E-mail addresses: gujincui@nimte.ac.cn (J. Gu), tao.chen@nimte.ac.cn (T. Chen), wangxun@mail.tsinghua.edu.cn (X. Wang), yanlk_79@hotmail.com (L. Yan).

https://doi.org/10.1016/j.cej.2022.135910
Received 28 December 2021; Received in revised form 21 February 2022; Accepted 17 March 2022
Available online 22 March 2022

performance for water purification.[10–13].

Photocatalysis is a green and sustainable technology for environmental remediation.[14–15] Coupling membrane filtration and photocatalysis have become a research hotspot for wastewater treatment.[16] Besides, the titanium dioxide nanoparticles (TiO_2 NPs) can be generated on the $Ti_3C_2T_x$ nanosheets, and the heterojunction can be formed.[13] It is anticipated that the TiO_2 NPs can endow the $Ti_3C_2T_x$ nanosheets with hydrophilicity and anti-fouling ability.[17] Based on these appealing properties, almost all the efforts are devoted to fabricating advanced MXene-based separation membranes with synergistically overall performances. For instance, Li et al. reported a 2D MXene/bismuth subcarbonate membrane for water purification.[3] The bismuth subcarbonate provided more channels for separation layers to enhance permeation flux and endowed this membrane with photocatalytic capacity. Sun et al. prepared a MXene-based lamellar membrane with high flux, self-cleaning (10 cycles), and stable separation ability under harsh conditions.[18] Lin et al. designed a TiO_2@MXene membrane with a flux recovery ratio of 80.2%~99.56% and an excellent self-cleaning function under UV irradiation.[19] However, the TiO_2 NPs usually have a wide bandgap, and their absorption of sunlight is limited to the UV range, so the energy utilization is insufficient. In addition, their photogenerated carrier migration process is usually prone to the compounding of electron-hole pairs. Hence, the photocatalytic efficiency will be decline. Therefore, achieving a wide range of sunlight absorption is crucial for efficient and sustainable wastewater purification. g-C_3N_4 nanosheets have received tremendous attention to design advanced membranes attributing their inherent merits. Recently, we presented an advanced g-C_3N_4-based membrane with excellent self-cleaning ability. It can realize continuous water purification with stable separation performance, catalytic degradation ability and antibacterial capacity, suggesting its potential value for optimizing the water environment.[16] Combining photocatalysis with specific structures will effectively solve the above problem.

Shells are the masterpiece of nature. They present 2D layered

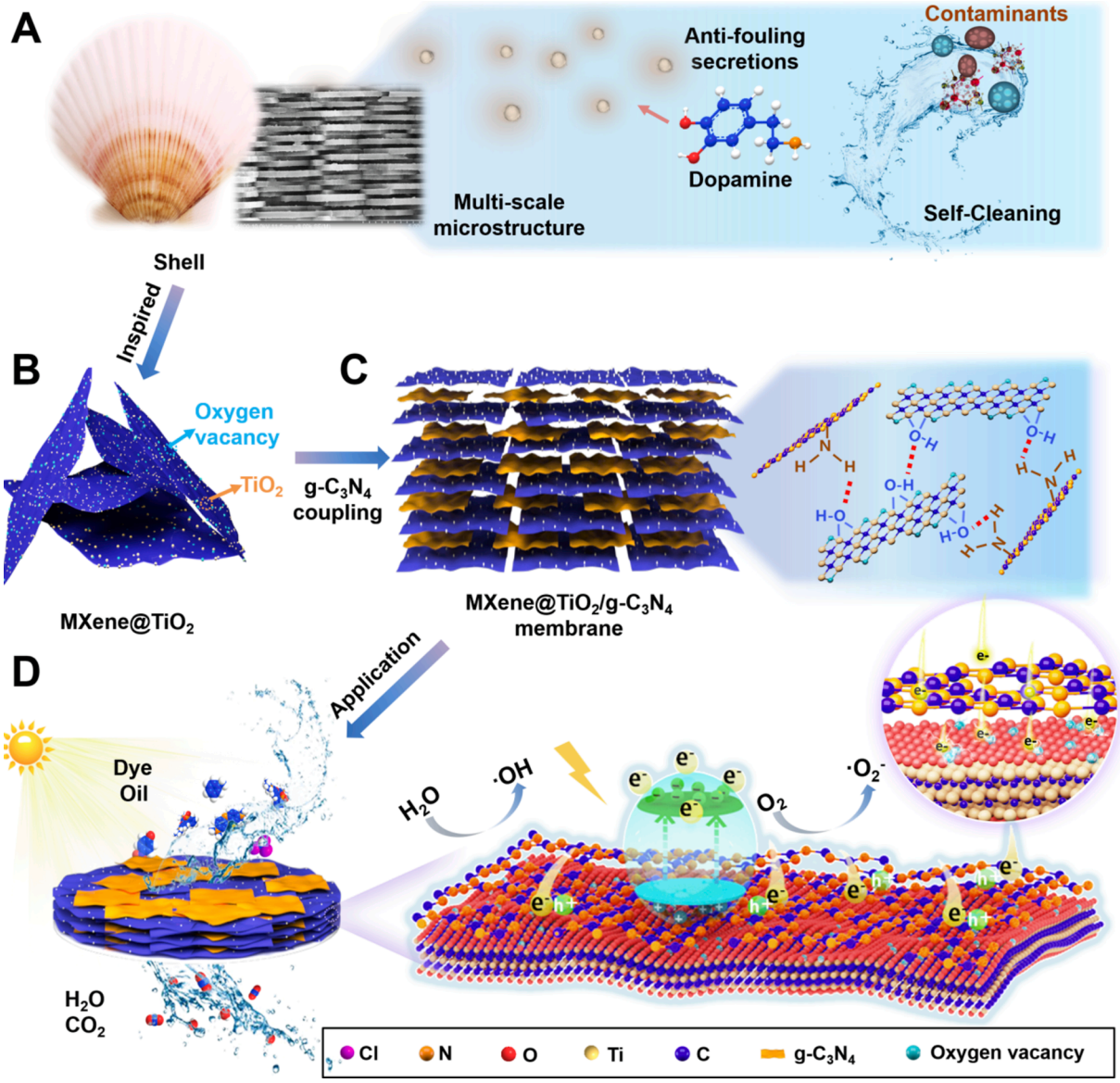

Fig. 1. Schematic illustration of the 0D/2D/2D MXene-based heterogeneous membrane fabrication through the solvothermal reaction and subsequent interface self-assembly. (A) Shells exhibit a stable structure and good self-cleaning ability due to the cross-stacked laminar structure and surface secretion of dopamine. (B) The 0D TiO_2 NPs and abundant oxygen vacancies were generated on the $Ti_3C_2T_x$ (MXene) nanosheets. (C) The MXene@TiO_2 nanosheets were combined with the g-C_3N_4 nanosheets through the interface self-assembly and hydrogen bonding. (D) Under the synergy of the oxygen vacancies, TiO_2 NPs, and g-C_3N_4 nanosheets, the obtained 0D/2D/2D MXene-based heterogeneous membrane presented excellent self-cleaning performance under sunlight for wastewater purification.

structures to give themselves good mechanical property. Moreover, they show good self-cleaning ability due to dopamine secretion.[20] Inspired by nature, here, by combining the advantages of the g-C_3N_4 and MXene nanosheets, we constructed an advanced 0D/2D/2D MXene-based heterogeneous layered membrane through solvothermal reaction and subsequent interface self-assembly (Fig. 1**A-1C**). Because of their thermodynamical metastability, the 0D TiO_2 nanoparticles (NPs) can be produced on the $Ti_3C_2T_x$ nanosheets (Fig. 1**B**). The TiO_2 NPs can broaden the transmission channel and endow the 0D/2D/2D heterogeneous membrane with anti-fouling ability. Meanwhile, abundant oxygen vacancies can be created on the $Ti_3C_2T_x$ nanosheets, trapping the photogenerated carriers, restraining charge recombination, and facilitating the effective spatial separation of electron-hole pairs (Fig. 1**B**).[21] Furthermore, the 0D/2D/2D heterojunction showed a broader sunlight-absorption ability than the origin g-C_3N_4 nanosheets and the $Ti_3C_2T_x$ nanosheets. Hence, the obtained 0D/2D heterojunction can increase the lifetime of the electron-hole pairs and expand the wavelength range of light response. Moreover, due to the synergy of the oxygen vacancies, TiO_2 NPs, and g-C_3N_4 nanosheets, the obtained heterogeneous membrane was endowed with a smaller bandgap (~2.27 eV) than most previous reports. This superior feature gives this membrane an excellent self-cleaning performance under sunlight. Therefore, it can maintain its original separation and photocatalytic degradation abilities with a more than 98% flux recovery ratio after the 45-times filtration experiment (Fig. 1**D**). Besides, it presented outstanding environmental stability under harsh water conditions. This work may provide a platform for building an advanced separation membrane with an excellent self-cleaning property for practical water purification.

2. Experimental

2.1. Materials

Ti_3AlC_2 (MAX) powder (~98%) was obtained from Jilin 11 Technology Co., Ltd. Lithium fluoride (LiF) was provided by Aladdin (Shanghai) Co., Ltd. Melamine and phosphorous acid were got from Tianjin Kemiou Chemical Reagent Co., Ltd. Hydrochloric acid (HCl) was provided by Tianjin Fengchuan Chemical Reagent Technology (Tianjin) Co., Ltd. Different contaminants molecules, including methylene blue (MB), p-nitrophenol (4-NP), tetracycline (TC), and rhodamine B (RhB) were bought from Aladdin (Shanghai) Co., Ltd. Different oils, including chloroform, toluene, was purchased from Aladdin Bio-Chem Technology Co., LTD. Benzoquinone (BQ), isopropanol (IPA), disodium EDTA (EDTA-2Na), bovine albumin (BSA), humic acid (HA), and alginic acid (AA) were bought from Aladdin (Shanghai) Co., Ltd. PVDF (pore: ~220 nm) was obtained from Millipore Industrial & Lab Chemicals. Others were got from Aladdin (Shanghai) Co., Ltd.

2.2. Fabrication of the $Ti_3C_2T_x$ (MXene) nanosheets.

$Ti_3C_2T_x$ (MXene) nanosheets were prepared based on the etching methods reported previously.[3] Firstly, LiF (1.6 g) was poured into HCl (9 mol/L, 20 ml) to prepare the etching solution. Secondly, the 1.0 g of Ti_3AlC_2 (MAX) powder was slowly added into the LiF-HCl etching solution in an ice bath and continued to stir for 36 h at 45 ℃. The $Ti_3C_2T_x$ (MXene) suspension was repeatedly washed with deionized water to pH greater than 6. The residue was diluted and sonicated under argon atmosphere for 2 h to peel the stacked nanosheets. The multilayer product was further removed by centrifugation at the suspension at 3500 rpm for 20 min. Finally, the $Ti_3C_2T_x$ (MXene) nanosheets were got by discarding the precipitate and freeze-drying for 20 h.

2.3. Fabrication of the g-C_3N_4 nanosheets.

The g-C_3N_4 nanosheets were fabricated by combining solvothermal and high-temperature sintering methods.[22] Firstly, 1.2 g of phosphorous acid and 1.0 g of melamine were dissolved in 100 ml DI water and stirred vigorously under 80℃ for 1 h. Secondly, the reaction solution was transferred to 150 ml of Teflon-lined autoclave under 180℃ for 10 h. Thirdly, the reactor was cooled to room temperature to release the pressure, and the product was washed with DI water and dried. The precursor (0.6 g) was placed in a mixture of glycerol (6 ml) and ethanol (18 ml), refluxed at 90℃ for 4 h with stirring. Finally, the g-C_3N_4 powders were heated at 500℃ in the air for 2 h. The g-C_3N_4 nanosheets were obtained as yellow powders.

2.4. Fabrication of the MXene@TiO_2 heterojunction and MXene@TiO_2/g-C_3N_4 heterojunction.

The $Ti_3C_2T_x$ (MXene) nanosheets and g-C_3N_4 nanosheets were added into water/ethanol (volume ratio = 1:1) mixed solution (60 ml) with varying mass ratios (1:0, 1:0.5, 1:1, 1:1.5). The mixture was sonicated and transferred to the Teflon-lined autoclave and hydrothermally reacted at 160℃ for 20 h. Lastly, the product was centrifuged, washed, and dried to obtain MXene@TiO_2 ($Ti_3C_2T_x$: g-C_3N_4 = 1:0), MXene@TiO_2/g-C_3N_4 ($Ti_3C_2T_x$: g-C_3N_4 = 1:0.5, 1:1, 1:1.5) heterojunctions, respectively.

2.5. Fabrication of the M, MC, MT, and MTC membranes.

The MXene, MXene/g-C_3N_4, MXene@TiO_2, and MXene@TiO_2/g-C_3N_4 membranes were prepared via vacuum-assisted self-assembly. Specifically, the MXene, MXene/g-C_3N_4, MXene@TiO_2, and MXene@TiO_2/g-C_3N_4 nanosheets were dispersed into the DI water (0.5 mg/ml) and ultrasound for 4 h, respectively. Then, the MXene, MXene/g-C_3N_4, MXene@TiO_2, and MXene@TiO_2/g-C_3N_4 dispersions with the same volume and concentration (0.5 mg/ml) were vacuum filtered onto the PVDF substrate under 0.2 bar. They were dried at room temperature for 15 h. The MXene membrane, MXene/g-C_3N_4 membrane, MXene@TiO_2 membrane, MXene@TiO_2/g-C_3N_4 membrane ($Ti_3C_2T_x$: g-C_3N_4 = 1:0.5, 1:1, 1:1.5) were marked as M membrane, MC membrane, MT membrane, MTC-0.5 membrane, MTC-1 membrane, MTC-1.5 membrane, respectively.

3. Results and discussion

The $Ti_3C_2T_x$ nanosheets were obtained by etching the Al layer of the Ti_3AlC_2 (MAX) in the LiF-HCl mixture.[4] Scanning electron microscopy (SEM) was performed to investigate the micromorphology change. As shown in **Figure S1**, the precursors Ti_3AlC_2 (MAX) presented a multilayer stacking state. However, after being etched, the interaction between the layers was weakened, and the $Ti_3C_2T_x$ nanosheets were obtained. The produced $Ti_3C_2T_x$ nanosheets presented an accordion-like structure and were split from each other, indicating the successful etching of the Ti_3AlC_2 (MAX) (Fig. 2**A**). Transmission electron microscopy (TEM) image revealed that the single-layer $Ti_3C_2T_x$ nanosheets were thin and almost transparent (Fig. 2**B**). At the same time, the lattice fringes with an interplanar space of 0.26 ± 0.001 nm can be observed from the high-resolution TEM (HRTEM), which was due to the (1 1 0) crystal face of $Ti_3C_2T_x$ nanosheets (Fig. 2**C**).[23].

Furthermore, the overall crystallinity of the Ti_3AlC_2 and $Ti_3C_2T_x$ nanosheets was studied through X-ray diffraction (XRD). The diffraction peak of the Ti_3AlC_2 (MAX) at 38.8° (1 0 4) disappeared, indicating the etching of Al (Fig. 2**D**).[24] Meanwhile, the (0 0 2) crystal plan shifted from 9.5° to 6.3°, intimating that Ti_3AlC_2 nanosheets had been successfully peeled off.[24] The average thickness of these $Ti_3C_2T_x$ nanosheets was ~ 1.67 nm, and their average lateral size was ~ 1.5 μm (Fig. 2**E-2F**). The high aspect ratio of the $Ti_3C_2T_x$ nanosheets reduced the meso- and macropores' presence and ensured the uniformity in the MXene-based membranes.[25].

The marginal titanium atoms can assume the role of the nucleating sites to generate the titanium dioxide nanoparticles (TiO_2 NPs).[26] Thereby, a $Ti_3C_2T_x$-based heterojunction can be facilely formed. As

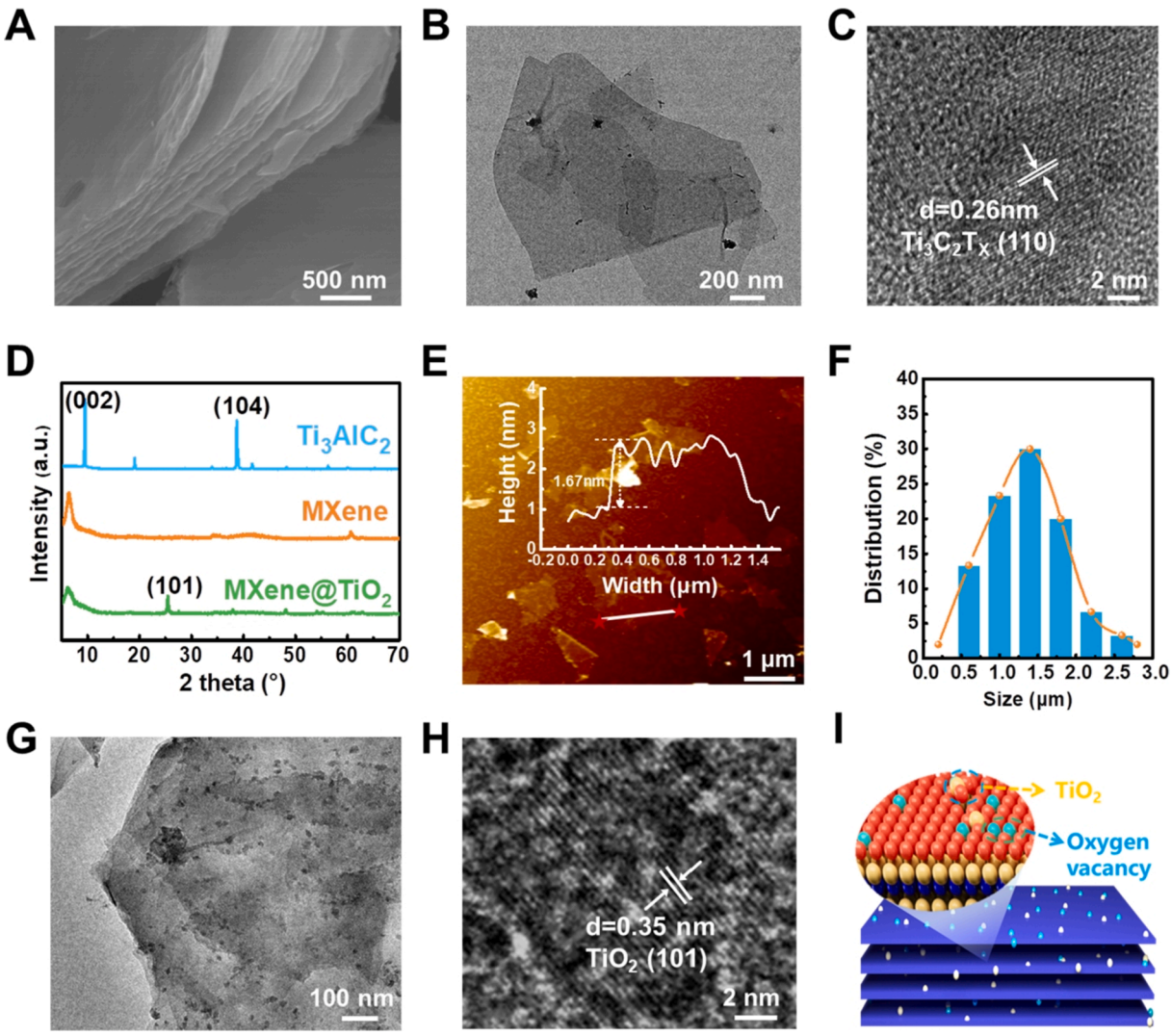

Fig. 2. (A) SEM image of the $Ti_3C_2T_x$ nanosheets. (B) TEM image of the $Ti_3C_2T_x$ nanosheets and its responding HRTEM image (C). (D) XRD patterns of Ti_3AlC_2 (MAX), single-layer $Ti_3C_2T_x$ (MXene), MXene@TiO_2 powers. (E) AFM image of the $Ti_3C_2T_x$ nanosheets and their responding thickness distribution. (F) The size distribution of the $Ti_3C_2T_x$ nanosheets. (G) TEM image of the MXene@TiO_2 nanosheets and the responding HRTEM image (H). (I) Schematic diagram of the generation process of the 0D TiO_2 NPs and abundant oxygen vacancies on the surface of the $Ti_3C_2T_x$ nanosheets due to the thermodynamical metastability of the $Ti_3C_2T_x$ nanosheets.

shown in **Figure 2D, a** new peak at 25.4° was observed on the MXene@TiO_2 (MT) heterojunction, which was resulted from the (1 0 1) crystal face of the TiO_2 NPs phase.[26] Besides, the TiO_2 NPs uniformly loaded on the $Ti_3C_2T_x$ nanosheets (Fig. 2**G**, **Figure S2**). The lattice fringes with a space of 0.35 ± 0.003 nm can be observed in the HRTEM, which was ascribed to the (1 0 1) plane of anatase TiO_2 NPs (Fig. 2**H**).[27] These results proved the co-existence of anatase TiO_2 and $Ti_3C_2T_x$ nanosheets. The introduction of TiO_2 NPs can effectively inhibit the individual $Ti_3C_2T_x$ nanosheets from stacking and accelerate the electron excitation.[28].

The growth mechanism of the formations of TiO_2 NPs may be as follows. During the wet chemical exfoliation process of MXene, Ti vacancy defects can be formed. Positively charged Ti vacancies can promote carbon oxidation in MXenes, resulting in producing more electron-hole pairs. Due to the high conductivity of the MXene, electrons easily aggregate on the MXene nanosheets unevenly, forming an internal electric field. Due to the accumulation of electrons, O_2 gains electrons to create $\cdot O_2^-$ into the lattice. Meanwhile, driven by the internal electric field, the Ti ions diffuse to the negative electrode and react with $\cdot O_2^-$ to form TiO_2 (Fig. 2**I**).[28] Moreover, the introduction of oxygen vacancies may be attributed to two reasons. On the one hand, the TiO_2 is reduced by the unoxidized Ti, resulting in oxygen absence and oxygen vacancies formation. On the other hand, the surface groups of MXene are changed during the solvothermal process. Partial –OH groups are removed, and vacancy defects at the O atoms are created.[29].

The microstructure of the g-C_3N_4 nanosheets was characterized through AFM and SEM. As displayed in **Figure S3**, the average lateral size of the g-C_3N_4 nanosheets was ~ 500 nm, much smaller than the $Ti_3C_2T_x$ nanosheets. The amorphous g-C_3N_4 nanosheets were anchored between MT layers, and the MXene@TiO2/g-C3N4 (MTC) heterojunction was built. Moreover, the TiO_2 NPs evenly decorated on the MTC heterojunction. Furthermroe, the introduction of g-C_3N_4 nanosheets formed hydrogen bonding (H-bonding) with the MT heterojunction, and did not alter the original lamellar structure of the $Ti_3C_2T_x$ nanosheets (Fig. 3**A**). The lattice distribution in the HRTEM image further demonstrated the tight interfacial contact of g-C_3N_4 with the MT (Fig. 3**B-3C**). Besides, there were two different lattices with 0.26 ± 0.001 nm and 0.35 ± 0.003 nm stripe widths. The former was representative of the (1 1 0) crystal plane of the MXene, and the latter was assigned to the (1 0 1) crystal plane of the TiO_2 (Fig. 3**C**).[23,27] In addition, a distinct amorphous structure can be observed (Fig. 3**C**), corresponding to the presence of g-C_3N_4 (**Figure S4**). The co-existence of the two lattice

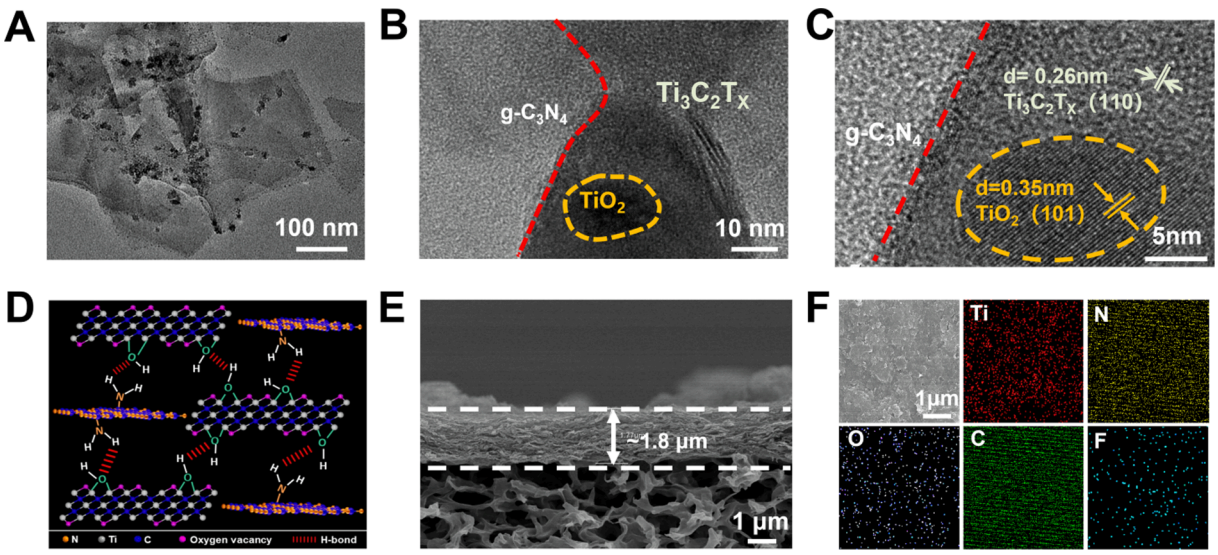

Fig. 3. (A) TEM image of MTC heterojunction. (B) TEM image of MTC heterojunction and its responding HRTEM image (C). (D) Schematic diagram of the interaction of the MT nanosheets and g-C_3N_4 nanosheets. (E) SEM image of a cross-section of the MTC membrane. (F) EDS maps of the MTC membrane.

fringes and the amorphous state confirmed the successful fabrication of the MTC heterojunction, benefiting from the H-bonding between the $Ti_3C_2T_x$ nanosheets and g-C_3N_4 nanosheets (Fig. 3**D**).[30] Fourier-transform infrared spectroscopy (FTIR) was used to prove the H-bonding formation. There was an apparent absorption peak at ~ 3300 cm^{-1}, attributed to the stretching vibrations of –OH (**Figure S5A**).[31] Compared with the MT membrane, the –OH stretching vibration peak of the MTC membrane became wider. A significant redshift occurred, indicating the generation of H-bonding between the MT and g-C_3N_4 nanosheets (**Figure S5B**).[32].

The MXene-based membranes were obtained through the vacuum-assisted interface assembly with an effective radius of ~ 2 cm (**Figure S6**). Fig. 3**E and Figure S7** showed the cross-section SEM image of the MTC membrane with a shell-like structure and a thickness of 1.8 ± 0.05 μm, which was higher than that of the MXene (M) membrane (0.8 ± 0.06 μm), MT membrane (1.0 ± 0.03 μm), MXene/g-C3N4 (MC) membrane (1.4 ± 0.09 μm) (**Figure S8**). Moreover, the $Ti_3C_2T_x$ nanosheets were stacked with g-C_3N_4 nanosheets in a well-aligned manner. Besides, the Energy Dispersive Spectroscopy (EDS) results proved the homogeneous distribution of the Ti, C, O, N elements in the MTC membrane (Fig. 3**F**), indicating the uniform combination of the $Ti_3C_2T_x$ nanolayers and g-C_3N_4 nanosheets. The differentiated lateral size was beneficial to build unique micro-pores and nano-pores and create additional transport channels for separation.[33] Moreover, the in-situ derivatization of TiO_2 NPs can support the interlayer between the $Ti_3C_2T_x$ nanosheets and g-C_3N_4 nanosheets, further improving the interfacial contact and extending the transport channels.[34].

The microstructure of the MXene-based membranes was further characterized through SEM. The MTC membrane was rougher than the others (Fig. 4**A**). This result was consistent with the responding atomic force microscopy (AFM) images (Fig. 4**B**, **Figure S9**). The enhanced roughness can facilitate the effective contact between membrane surface and contaminants to expose more active sites for solar energy utilization.[35,36].

X-ray photoelectron spectroscopy (XPS) was further carried out to analyze the chemical characterization of these membranes. As shown in Fig. 4**C**, four elements C, Ti, O, and F existed on the M membrane. However, the F 1 s peak disappeared in the XPS curves of the other membranes, indicating the substitution of Ti-F groups during the heterojunction formation.[37] Moreover, a clear N 1 s peak appeared in the MC membrane and MTC membrane, indicating the successful introduction of g-C_3N_4 (Fig. 4**C**). Furthermore, the Ti 2p spectrum of the M membrane was divided into eight peaks, locating at 464.4 eV, 462.7 eV, 462.1 eV, 461.0 eV, 458.9 eV, 456.4 eV, 455.4 eV, 454.8 eV, which were corresponded to Ti(IV), Ti(III), Ti(II) and Ti-C bonds of $2p^1$ and $2p^3$ orbitals, respectively (Fig. 4**D**).[38] In addition, compared to the M membrane, the intensity of the low-valence Ti peak in the MTC membrane weakened, which indicated a redox reaction occurred during the formation of heterojunction (Fig. 4**D**).[39] The lower valence Ti compounds were more reductively active, and therefore could be easily consumed as an electron donor for the reduction reaction.[39] Besides, the Ti(IV) peak of the MTC membrane moved to lower binding energy compared to the M membrane (Fig. 4**D**). This phenomenon confirmed the directional migration of electrons from g-C_3N_4 nanosheets to $Ti_3C_2T_x$ nanosheets.[37] Additionally, the N 1 s spectrum in the g-C_3N_4 and MTC membranes was divided into three peaks assigned to N-NH_2, N-$(C)_3$, and C-N = C (Fig. 4**E**).[40] The overall shift of the N 1 s peak in the MTC membrane toward the high binding energy further indicated the tight interfacial contact and electron transport between g-C_3N_4 and $Ti_3C_2T_x$ nanosheets.[41] Besides, compared to the g-C_3N_4 membrane, the N-C = N bond in the C 1 s XPS spectrum of the MTC membrane shifted positively, confirming the formation of MTC heterojunctions (**Figure S10**).[23].

Moreover, the MTC membrane became more affinities to water owing to the micro-scale multilayer structure and hydrophilic functional groups.[42] Furthermore, the WCA of the MTC membrane attained 36.4 ± 2.26° with the mass ratio of the $Ti_3C_2T_x$ and g-C_3N_4 being 1:1 (Fig. 4**F**). The water droplet quickly passed through the MTC-1 membrane within ~ 9 s, which was faster than the M membrane (281 ± 15 s), MC membrane (17 ± 2 s), and MT membrane (14 ± 1 s) (**Movie S1-S4**). Meanwhile, the MTC-1 membrane presented underwater super-oleophobicity property toward all the investigated oils with contact angles above 150° compared with the other membranes (Fig. 4**G, Figure S11**). Therefore, in the dynamic adhesion test, the oil droplet quickly detached once being contacted with the surface of the MTC-1 membrane because of the hydration water layer on the solid/water/oil three-phase interface (**Figure S12**).[43] Besides, the MTC-1 membrane displayed corrosion resistance ability if being immersed in the hydrochloric acid (HCl), sodium hydroxide (NaOH), and sodium chloride (NaCl) solutions, respectively. The underwater oil contact angle for the MTC-1 membrane was maintained above 150° under these strict conditions for 24 h, indicating its excellent environmental stability (Fig. 4**H**).

Oxygen vacancies (O_V) can also be generated along with the TiO_2

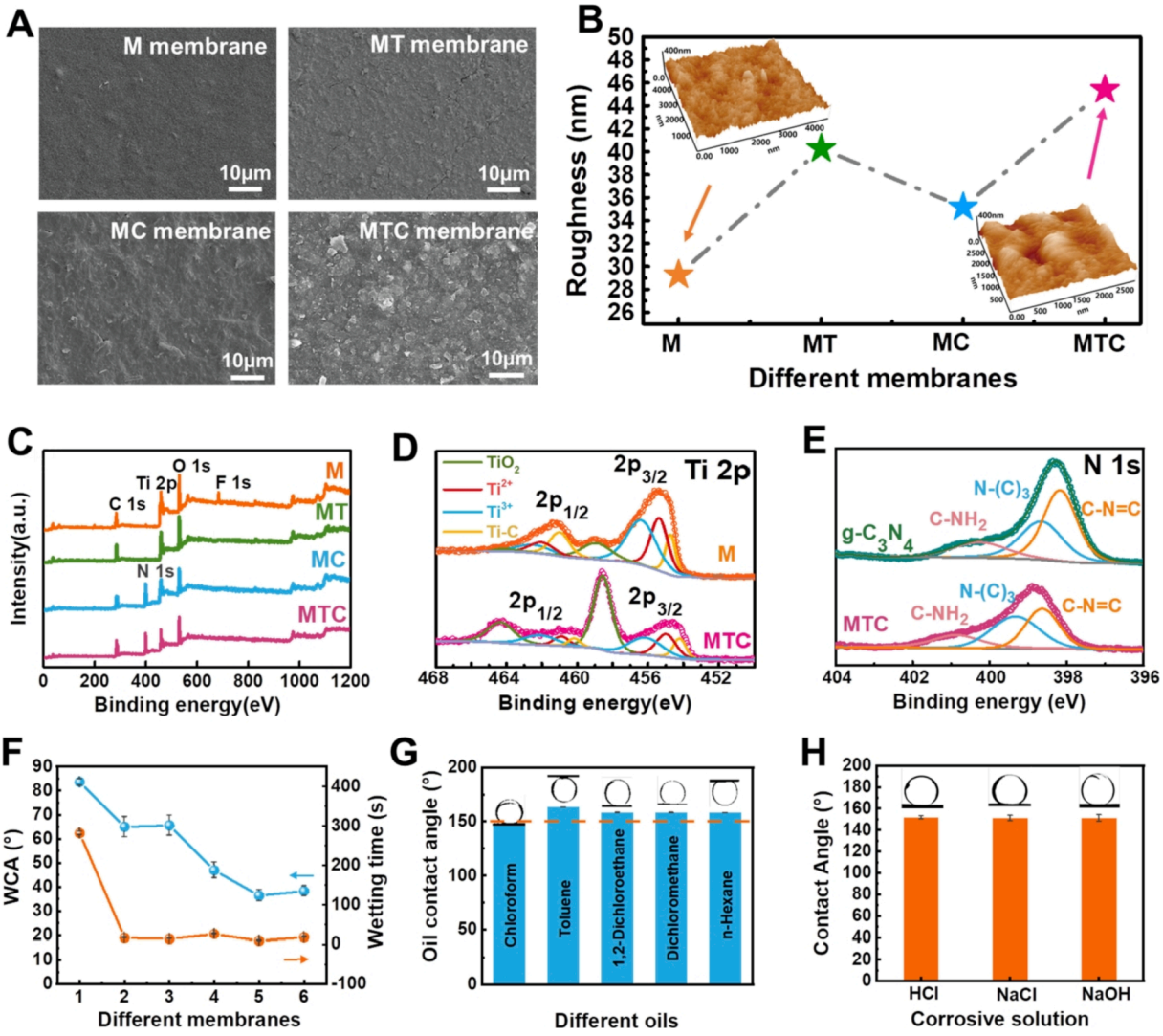

Fig. 4. (A) SEM images of the M membrane, MT membrane, MC membrane, and MTC membrane, respectively. (B) The roughness results of the M membrane, MC membrane, MT membrane, and MTC membrane, respectively. (C) XPS spectra of the M membrane, MC membrane, MT membrane, and MTC membrane, respectively. (D) Ti 2p XPS spectra with the fitting results of the M membrane and MTC membrane. (E) N 1 s XPS spectra with the fitting results of the g-C_3N_4 and MTC membranes. (F) Water contact angle (5 s) and wetting time of different membranes (1-M membrane, 2-MC membrane, 3-MT membrane, 4-MTC-0.5 membrane, 5-MTC-1 membrane, 6-MTC-1.5 membrane). (G) The underwater oil contact of the MTC-1 membrane for various oils. (H) The underwater contact angles of the MTC-1 membrane for chloroform after immersion in different environments for 24 h.

NPs due to the thermodynamical metastability of the $Ti_3C_2T_x$ nanosheets.[21] As shown in **Figure 5A, a** distinct characteristic peak can be observed at ~ 531.6 eV, indicating the presence of O_V in the MTC membrane.[44] The binding energies at ~ 532.8 eV and ~ 529.8 eV in the O 1 s XPS spectrum corresponded to the chemically adsorbed oxygen (O_C) and lattice oxygen (O_L), respectively.[45] Moreover, the room temperature electron paramagnetic resonance (EPR) confirmed the abundant O_V in the MTC membrane.[15] As shown in Fig. 5**B**, the MTC membrane rather than the M membrane and MT membrane displayed a distinctive sign with the g value of 2.004, which was related to the unpaired electrons' typical signals OV in the MTC membrane.[44,46] Furthermore, there was almost no change, even changing the content ratio of the g-C_3N_4 in the MTC membrane. The introduction of O_V was also proved through the UV–vis diffuse reflectance. The M and MC membranes exhibited plateauing optical absorption from 230 to 700 nm because of the unique optical absorption properties of MXene (Fig. 5**C**).[47] The MT membrane revealed a significant absorption threshold ~ 400 nm, attributing to the intrinsic absorption of TiO_2 NPs.[46] In addition, the oxygen atoms were removed from the crystal lattice after O_V formation. The excess electrons were captured by the surrounding metal atoms, thereby changing the orbital structure, narrowing the bandgap width of the material, and improving light absorption. Therefore, the MTC membrane displayed extended absorption in the 400 ~ 700 nm range.[15] These results were consistent with that of the XPS and EPR spectrum. Besides, the absorption edge of the MTC membrane displayed a redshift compared to the other membrane (Fig. 5**C**).[26] This change endowed the MTC membrane with enhanced visible-light absorptive ability.

Based on the UV–vis diffuse reflectance spectrum, the bandgaps of these membranes were calculated through the Kubelka-Munk method. As shown in **Figure S13**, the M membrane exhibited a flat absorption, and the bandgap was ~ 0.09 eV, which was consistent with the previous report.[48] Moreover, due to the g-C_3N_4 introduction, the MC membrane showed a smaller absorption peak at ~ 400 nm, resulting in a bandgap of ~ 0.47 eV. Nevertheless, the electron-hole pairs easily recombined among these two membranes.[23] The bandgap of the MT membrane was ~ 2.54 eV. After introducing the g-C_3N_4 nanosheets into the MT membrane, the bandgap of the MTC membrane was ~ 2.27 eV, which was smaller than the pure g-C_3N_4 membrane (~2.78 eV) (Fig. 5**D**). The Mott-Schottky curve further investigated the bandgap.

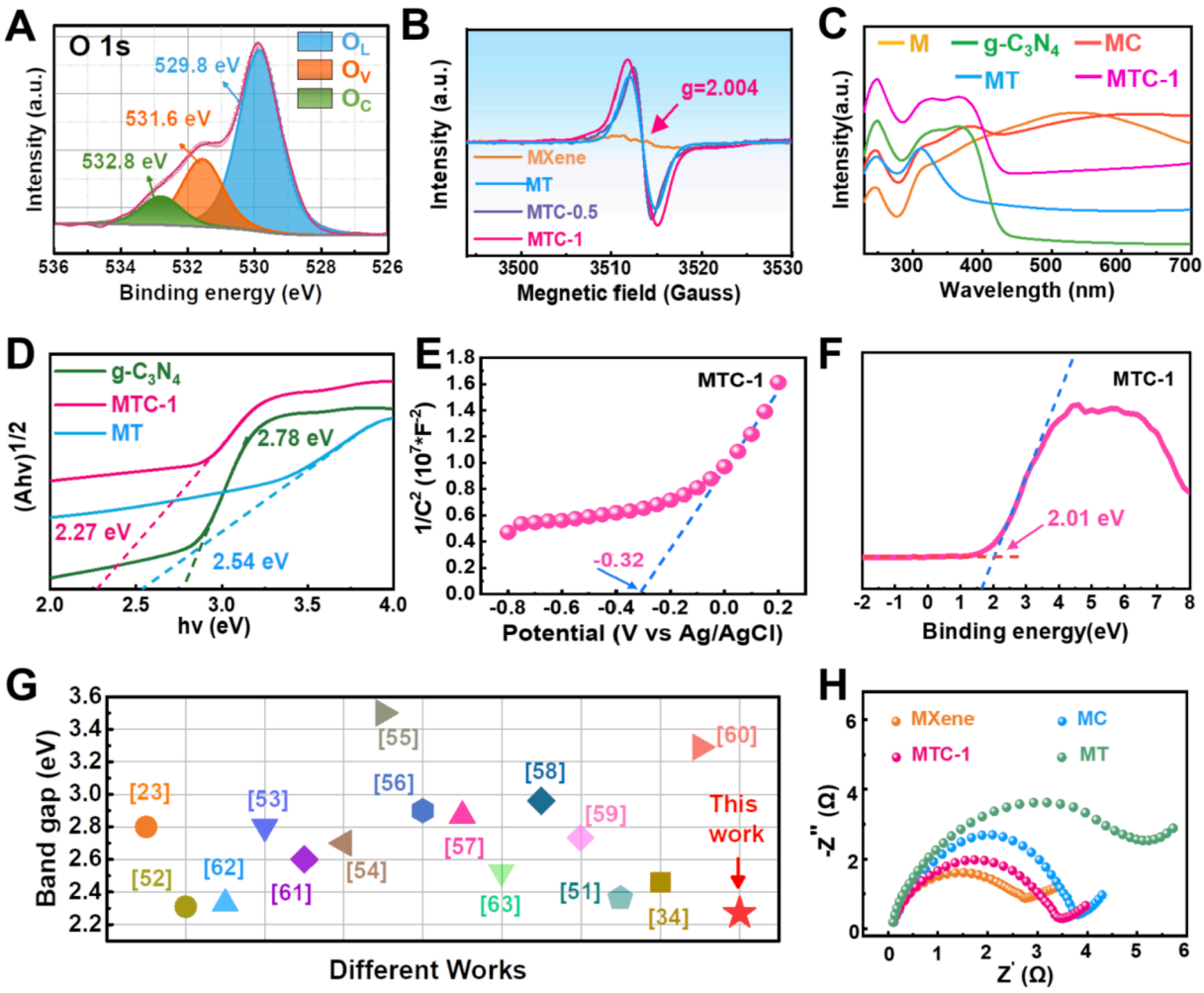

Fig. 5. (A) O1s XPS spectra of the MTC membrane. (B)EPR spectra of the M, MT, MTC-0.5, and MTC-1 membranes. (C) UV–vis absorption spectra of M membrane, g-C_3N_4 membrane, MC membrane, MT membrane, and MTC membrane. (D) Plots of $(Ah\nu)^{1/2}$ versus $h\nu$ of the g-C_3N_4 membrane, MT membrane, and MTC-1 membrane. (E) Mott-Schottky plots of MTC-1 membrane. (F) XPS valence band spectrum of MTC-1 membrane. (G) Bandgap comparison of different MXene-based and g-C_3N_4 based heterojunctions previously reported and this work. (H) EIS spectra of the M, MT, MC, MTC-1 membrane.

The slope of the linear part was positive, indicating the MTC was an n-type semiconductor (Fig. 5**E**). The flat-band potential of MTC relative to the Ag/AgCl electrode was about −0.32 V, and the conduction band (CB) potential of the MTC was about −0.42 V. According to the standard electrode potential of Ag/AgCl, the CB potential of MTC under standard hydrogen electrode was about −0.22 V (E_{CB}). Besides, XPS was applied to measure the valence band (VB) of the MTC-1 membrane. As shown in Fig. 5**F**, the VB of MTC was ~ 2.01 eV (E_{VB}). According to $E_g = E_{VB}$-E_{CB}, the E_g of the MTC-1 membrane was ~ 2.23 eV, which was close to the E_g obtained by the Kubelka-Munk method (~2.27 eV). The lower bandgap of the MTC membrane was due to the optimized electronic band structure and the oxygen vacancies introduction during the formation of the MTC heterojunction.[49,50] Moreover, the bandgap of the MTC membrane was smaller than the majority of previous works (Fig. 5**G**). [23,34,51–63] These features will endow the MTC membrane with high sunlight absorption capacity and excellent photocatalytic degradation performance for contaminations under sunlight (**Table S1**).[63].

The electrochemical impedance spectroscopy (EIS) was further applied to investigate the electron mobility of each membrane. As shown in Fig. 5**H**, the MXene membrane has the smallest radius, indicating that MXene has higher electrical conductivity. The excellent electrical conductivity made the MXene membrane a good electron-accepting platform, which promoted charge separation.[64] Besides, compared with the MC and MT membranes, the MTC-1 membrane has a smaller radius, indicating that the heterojunction is beneficial to reduce the interfacial charge transfer resistance, accelerate the migration of photogenerated carriers, thereby improving the photocatalytic performance of the MTC-1 heterojunction.[65].

The special wettability made the MTC membrane a good choice for water purification. As shown in **Figure S14A**, the MTC-1 membrane presented an excellent separation capacity for chloroform-in-water (C/W) emulsion, toluene-in-water (T/W) emulsion, 1, 2-dichloroethane-in-water (D/W) emulsion, dichloromethane-in-water (DM/W) emulsion, n-hexene-in-water (H/W) emulsion, with the efficiency of 98.4 ± 0.3%, 99.4 ± 0.4%, 94.4 ± 0.4%, 98.5 ± 1.5%, 96.5 ± 0.9%, respectively. Furthermore, the separation flux of the MTC-1 membrane for C/W emulsion was higher than that of the other membranes (**Figure S14B**). The M membrane showed a lower separation flux of 36.7 ± 2.9 L $m^{-2}h^{-1}$ bar^{-1} because of the tightly stacked and narrow channels of the $Ti_3C_2T_x$ nanosheets. However, after introducing the g-C_3N_4 nanosheets, a "defective" layer stack was created, and thus an effective diffusion path for mass transfer was provided.[4] Similarly, the in situ-growth TiO_2 NPs can be acted as a 0D nano-support to construct unique interlayer channels with a loose structure.[49] Hence, the separation flux of MC and MT membranes increased to 52.1 ± 3.4 L $m^{-2}h^{-1}$ bar^{-1} and 103.1 ± 10.7 L $m^{-2}h^{-1}$ bar^{-1}, respectively. Furthermore, by coupling the TiO_2 NPs and g-C_3N_4 nanosheets, the separation flux of the MTC-1 membrane attained 231.8 ± 27.2 L $m^{-2}h^{-1}$ bar^{-1} (**Figure S14B**). In addition,

optical microscopy and dynamic light scattering measurement (DLS) were also performed to evaluate the separation ability of the MTC-1 membrane. As displayed in **Figure S15**, the filtration was almost transparent and different from the milky-white feed with a size larger than 100 nm. In addition, the cyclic separation performance of the MTC-1 membrane was evaluated. There was no remarkable change after the 45-times cycles separation process, indicating the excellent separation performance of the MTC-1 membrane (Fig. 6**A**).

The self-cleaning performance was also studied through the sequential "water-C/W emulsion-water-water" process. The initial water fluxes (J_0) of the M, MC, MT and MTC-1 membranes were 859 ± 46 L $m^{-2}h^{-1}$ bar^{-1}, 986 ± 43 L $m^{-2}h^{-1}$ bar^{-1}, 4479 ± 332 L $m^{-2}h^{-1}$ bar^{-1}, 13016 ± 2494 L $m^{-2}h^{-1}$ bar^{-1}, respectively (Fig. 6**B**). However, the C/W emulsion fluxes (J_1) of these membranes decreased sharply into 39.3 ± 0.6 L $m^{-2}h^{-1}$ bar^{-1}, 54.0 ± 1.0 L $m^{-2}h^{-1}$ bar^{-1}, 121.3 ± 8.3 L $m^{-2}h^{-1}$ bar^{-1}, 246.3 ± 18.7 L $m^{-2}h^{-1}$ bar^{-1}, respectively (Fig. 6**B**). Even after alternative cleaning with water and ethanol, the water fluxes (J_2) of these membranes only recovered to 305.0 ± 15.5 L $m^{-2}h^{-1}$ bar^{-1}, 570.3 ± 32.2 L $m^{-2}h^{-1}$ bar^{-1}, 2703.3 ± 198.2 L $m^{-2}h^{-1}$ bar^{-1}, 4945.0 ± 354.9 L $m^{-2}h^{-1}$ bar^{-1}, respectively (Fig. 6**B**). Excitingly, after sunlight irradiation, the water fluxes (J_3) of the MTC-1 membrane recovered to 12754.7 ± 2520.8 L $m^{-2}h^{-1}$ bar^{-1}. However, the water fluxes (J_3) of M, MC, MT membranes were only 363.3 ± 13.4 L $m^{-2}h^{-1}$ bar^{-1}, 73 ± 25. 9 L $m^{-2}h^{-1}$ bar^{-1}, 3001.34 ± 171.78 L $m^{-2}h^{-1}$ bar^{-1}, respectively (Fig. 6**B**).

Furthermore, these membranes' contamination ratio (R) and the flux recovery ratio (FRR) were evaluated on the water flux during the continuous separation process. As shown in Fig. 6**C**, the total contamination ratio (R_t) of M, MC, MT, and MTC-1 membranes was more than 90% due to the high concentration of C/W emulsion and the narrow 2D laminar structure. After illumination with sunlight, the flux recovery of M, MC, and MT membranes was only 42.0 ± 2.6%, 74.4 ± 1.8%, and 67.1 ± 2.4%, whereas the flux recovery of MTC-1 membrane attained to 98.0 ± 0.6%. In addition, the MTC-1 membrane showed the lowest irreversible fouling ratio (R_{ir}) of ~ 2% compared with the M membrane (57.6 ± 2.6%), MC membrane (25.6 ± 1.8%), and MT membrane (32.9 ± 2.4%).

The excellent self-cleaning ability of the MTC-1 membrane was due to the synergy of the hydration and the photocatalytic degradation effects.[66] For one thing, the superhydrophilicity of the MTC-1

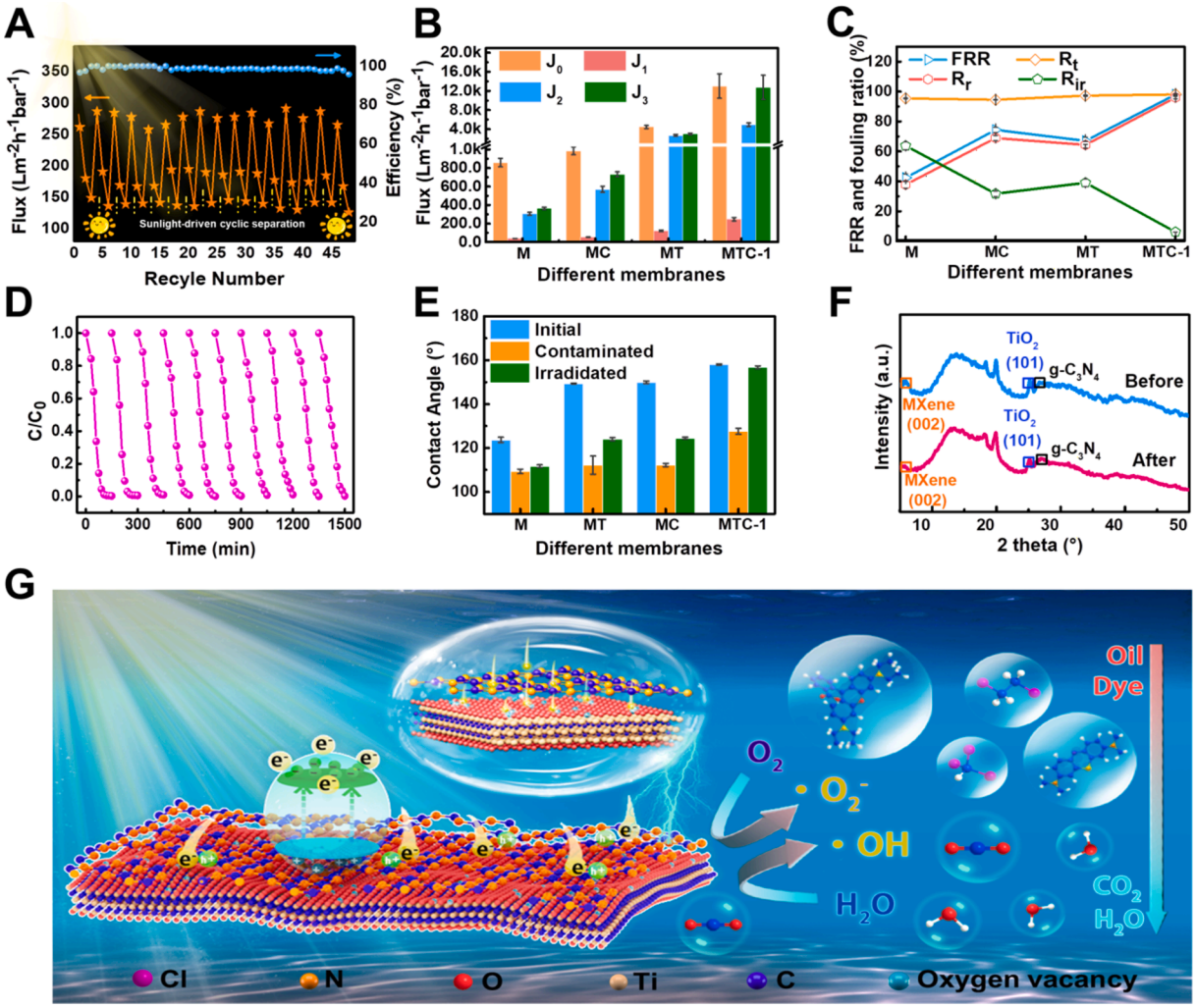

Fig. 6. (A) The cyclic separation performance of the MTC-1 membrane for C/W emulsion after being irradiated with sunlight. (B) The initial and recovery flux of the M membrane, MC membrane, MT membrane, and MTC-1 membrane (J_0: initial water flux, J_1: separation flux of C/W emulsion, J_2: water flux after being washed with water and ethanol, J_3: water flux after being irradiated under sunlight). (C) The flux recovery ratio (FRR), the total fouling ratio (R_t), irreversible fouling ratio (R_{ir}), and reversible fouling ratio (R_r) of the M membrane, MC membrane, MT membrane, and MTC-1 membrane, respectively. (D) The cyclic photocatalytic degradation performance of MTC-1 membrane for RhB solution under sunlight. (E) Chloroform contact angle of different membranes under different stages, including the initial, contaminated, and irradiation under sunlight. (F) XRD results of the MTC-1 membrane before and after photocatalytic degradation. (G) Photocatalytic degradation mechanism of the MTC-1 membrane.

membrane effectively inhibited the oil droplets from adhering to its inner/outer surface.[67] For another, the heightened visible light absorption performance of the MTC-1 membrane with a small bandgap (~2.27 eV) can endow this membrane with superior self-cleaning ability.[16] In addition, Rhodamine B (RhB) was selected as the target pollutant to systematically survey the catalytic degradation ability of the MTC heterogeneous membrane under simulated sunlight. The dark reaction was conducted for 0.5 h to reach adsorption–desorption equilibrium (Figure S16). The photocatalytic degradation performance of these membranes was shown in Figure S17A. The M membrane displayed lower photocatalytic degradation ability with 37.4 ± 4.6% efficiency in 120 min. As to the MT and MC membranes, the photocatalytic degradation efficiencies improved 49.2 ± 7.3% and 96.4 ± 1.6%, respectively. However, regarding the MTC-1 membrane, the degradation efficiency enhanced to 99.7 ± 0.2% after 90 min. The excellent photocatalytic performance of the MTC-1 membrane was attributed to the synergy of the roughness and smaller bandgap.[60] The former increased specific surface area to expose more reactive sites to decompose pollutants.[68] The latter was beneficial to broadening the photoresponse range for continuous and efficient photocatalysis. Moreover, both the MTC-0.5 and MTC-1.5 membranes presented lower photocatalytic efficiency. On the one hand, the small $Ti_3C_2T_x$ nanosheets brought fewer charge transfer platforms. On the other hand, excessive $Ti_3C_2T_x$ nanosheets can cover the active sites via shading effect, resulting in weaker photocatalytic efficiency.[16].

A pseudo-first-order kinetic equation with a linear fit of $\ln(C_0/C)$ against time was further surveyed the photocatalytic abilities of these membranes. Three-stage kinetics process showed in these membranes. The apparent rate constant increased during the photocatalytic degradation process of RhB due to the decrease of the reflection and refraction of incident sunlight.[69] The maximum photodegradation rate constant of the MTC-1 heterogeneous membrane was ~ 0.061 min^{-1} in the second stage, which was 2.9 times and 12.2 times higher than that of the MC (~0.021 min^{-1}) and MT membrane (~0.005 min^{-1}) (Figure S17B). Furthermore, a UV–vis spectrophotometer was explored to survey the photocatalytic degradation capacity of these membranes. As shown in **Figure S17C**, there was a significant decrease in the maximum absorbance (λ_{max}) of M membrane for RhB (~554 nm) at the dark reaction stage. The curve almost overlapped after turning on the light, indicating the adsorption process of the RhB molecules. However, as to the MC, MT, and MTC-1 membranes, the λ_{max} moved to a short wavelength, revealing the photocatalytic reaction occurred, and the by-products were generated. Especially for the MTC-1 membrane, the λ_{max} gradually blue-shifted from ~ 554 nm to ~ 495 nm, which was resulted from the N-de-ethylation and the breakage of the conjugate structure of the RhB molecule.[69].

The continuous decomposition of RhB also evaluated the stability of the MTC-1 membrane. As shown in Fig. 6**D**, this membrane maintained a high RhB degradation efficiency (greater than95%) after 10 cycles of degradation, demonstrating the excellent photocatalytic degradation performance of the MTC-1 membrane under sunlight. In addition, the MTC-1 membrane maintained its initial wettability with an underwater chloroform contact angle of 157.7°± 0.3° only after the irradiation of the sunlight (Fig. 6**E**). This result was superior to the other membranes, including M membrane, MT membrane, MC membrane (Fig. 6**E, Figure S18**). Besides, the MTC-1 membrane kept its initial XRD state even after 10 cycles of photocatalytic degradation that the peaks at ~ 5.20°, ~25.10°, ~26.67° assigned to the characteristic diffraction peaks of MXene (0 0 2), TiO_2 (1 0 1), and g-C_3N_4, respectively (Fig. 6**F**).[24,26] In addition, the MTC-1 membrane kept its initial XPS spectra after the photocatalytic degradation (**Figure S19**). The MTC-1 membrane also displayed excellent photocatalytic degradation ability for others, such as methylene blue (MB), with an efficiency of 99.5% (**Figure S20-S21**), further indicating its potential application for water treatment.

Apart from dye molecules, p-Nitrophenol (4-NP) and tetracycline (TC) are priority toxic pollutants in wastewater. It is not easy to eliminate these contaminations because of their stable chemical structure. However, animal investigations suggested that they can cause a blood disorder and bring environmental risks to human health. Therefore, removing these pollutants from water has aroused many interests. This work studied the photocatalytic degradation ability of the MTC-1 membrane for 4-NP and TC. As shown in Figure S20 and Figure S22, the degradation efficiency of the 4-NP (10 ppm) solution and TC (20 ppm) attained 86.9 ± 3.4% and 92.1 ± 2.9%, respectively, indicating its general photocatalytic degradation performance under sunlight. In addition, the MTC-1 membrane showed superior self-cleaning performance (**Figure S23A-S23C**). The initial separation flux of the MTC-1 membrane for alginic acid (AA) solution was 379 L ± 25 $m^{-2}h^{-1}$ bar^{-1}. After continuous fouling with the AA solution, the separation flux sharply declined to 284 ± 14 L $m^{-2}h^{-1}$ bar^{-1} in the second stage and 204 ± 9 L $m^{-2}h^{-1}$ bar^{-1} in the third stage, respectively (**Figure S23A**). This apparent change was due to the enrichment of the AA molecules and membrane fouling. However, even after five cycles of contamination tests, there was only a slight decrease in the membrane flux after sunlight irradiation. Similarly, the MTC-1 membrane presented a good excellent self-cleaning performance for humic acid (HA) and bovine serum albumin (BSA), with the separation *FRR* of 98.3 ± 0.5% and 99.5 ± 0.4%, respectively (**Figure S23B-S23C**). Furthermore, the performance of the MTC-1 membrane was better than that of most of the previous works (**Table S2**). The superior performance indicated that the MTC-1 membrane has an excellent photocatalysis ability for membrane fouling control and favorable reusability.

Based on the discussion above, the photocatalytic degradation mechanism of the MTC-1 membrane for various pollutants is described in Fig. 6**G**.[70,71] Under sunlight irradiation, the electrons on the MTC-1 membrane are excited when the photon energy ($h\nu$) is larger than the energy gap of the MTC-1 membrane. Then, the stimulated photoinduced electron (e^-) transfers from the valence band to the conduction band. Thereby the photoinduced positive hole (h^+) is generated (MTC-1 + $h\nu$ → $h^+ + e^-$). Subsequently, the produced e^- and h^+ are highly separated and move to the different positions of the MTC-1 membrane. Meanwhile, the MXene can cause the e^- to migrate to its surface, facilitating the effective spatial separation of photogenerated carriers. Lastly, the h^+ reacts with water and generates hydroxyl radicals (·OH), which can degrade the pollutants on the surface of the MTC-1 membrane into CO_2 and H_2O ($h^+ + H_2O$ →·OH; ·OH + pollutants → $CO_2 + H_2O$). At the same time, the e^- produces active $\cdot O_2^-$ and degrades the contaminations into CO_2 and H_2O through the redox reaction ($e^- + O_2$ →$\cdot O_2^-$; $\cdot O_2^-$ + pollutants → $CO_2 + H_2O$). [70].

A quenching test was supplemented to demonstrate the formation of free radicals. Different scavengers, including benzoquinone (BQ), isopropanol (IPA), and disodium EDTA (EDTA-2Na) with a concentration of 1 mmol/L, were added to the RhB solution, respectively during the photocatalytic degradation measurement. The EDTA-2Na had no noticeable inhibitory effect on the catalytic degradation ability of the MTC-1 membrane with an efficiency greater than 90%. However, after adding the BQ and IPA, the degradation efficiency of the MTC-1 membrane decreased from 99.7 ± 0.2% to 47.7 ± 2.2% and 84 ± 2.1%, respectively (Fig. 7**A**). In addition, the rate constants of RhB degradation by MTC-1 membrane decreased from 0.062 min^{-1} to 0.013 min^{-1} and 0.004 min^{-1} (Fig. 7**B**). These results indicated that $\cdot O_2^-$ and ·OH are the main active species during the photodegradation process, and the redox pathway initiated by $\cdot O_2^-$ was dominant. EPR test was further applied to verify the photocatalytic function of the MTC-1 membrane. As shown in Fig. 7**C-7D**, the characteristic peak of ·OH with the intensity ratio of 1:2:2:1 and the characteristic peak of $\cdot O_2^-$ with the intensity ratio of 1:1:1:1 appeared. Furthermore, the distinct intensity of characteristic peaks was enhanced with increasing illumination time. These results proved the existence of ·OH and $\cdot O_2^-$ during the photocatalytic process, which was consistent with the results of the quenching test. Several reasons can explain the enhanced photocatalytic degradation of the MTC-1 membrane. On the one hand, the lower bandgap of the MTC-1

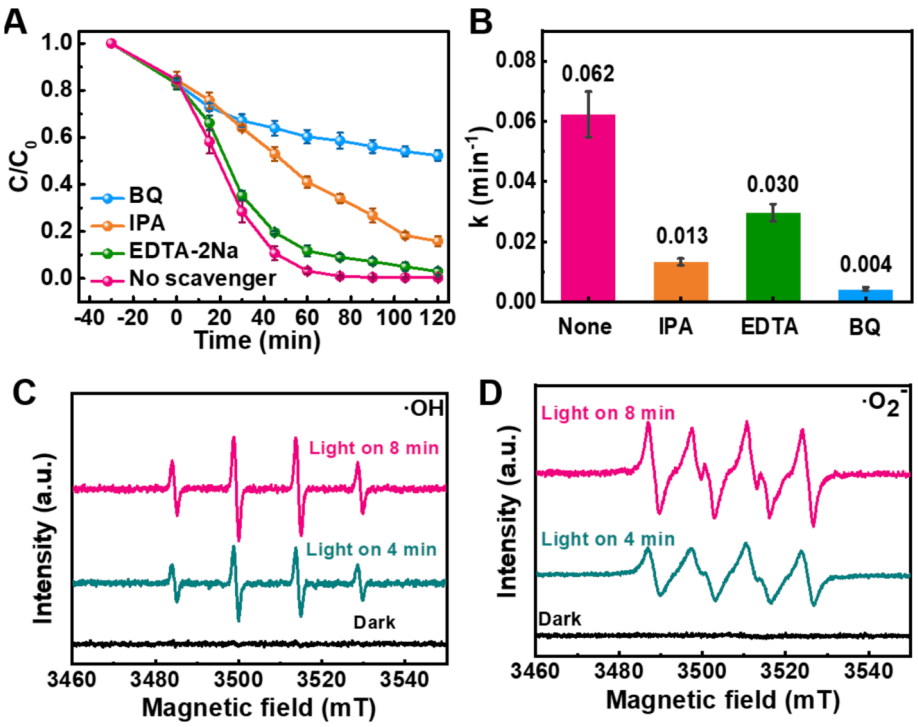

Fig. 7. Catalytic degradation curves (A) and corresponding kinetic constants (B) for quenching of reactive radicals. (C-D) EPR test for free radical trapping of MTC materials under dark and light.

membrane can improve the light absorbance ability and broaden the absorbent range, providing more e^--h^+ pairs and promoting their effective separation. On the other hand, the oxygen vacancies in the MTC-1 membrane can capture the electrons on the CB, which can prolong the photogenerated carrier lifetime.[71] Under the collection of oxygen vacancies and ·OH and $\cdot O_2^-$, the MTC-1 membrane presented an outstanding self-cleaning performance.

4. Conclusion

In summary, inspired by nature, an advanced 0D/2D/2D MXene-based heterogeneous membrane was constructed under the synergy of graphitic carbon nitride (g-C_3N_4) and $Ti_3C_2T_x$ nanosheets. The 0D TiO_2 NPs and oxygen vacancies were generated because of the thermodynamical metastability of the $Ti_3C_2T_x$ nanosheets. The produced TiO_2 NPs can broaden the transmission channel and endow this membrane with anti-fouling ability. Meanwhile, the oxygen vacancies can capture the photogenerated electrons and accelerate the practical separation of electron-hole pairs. Furthermore, by coupling the g-C_3N_4 nanosheets and TiO_2 NPs, the 0D/2D/2D heterogeneous membrane displayed a broader light absorption ability than the origin g-C_3N_4 and the $Ti_3C_2T_x$ nanosheets. Benefiting from the collaboration of the oxygen vacancies, TiO_2 NPs, and g-C_3N_4 nanosheets, the MXene-based heterogeneous membrane showed a smaller bandgap (~2.27 eV) than most previous reports. These features endowed this membrane with excellent self-cleaning ability under sunlight. Therefore, this membrane kept its emulsion separation and catalytic degradation capacities with *FRR* more than 98% after the 45-times experiment. This work will offer a novel approach to constructing 2D membranes with sunlight-driven self-cleaning performance to achieve sustainable water purification.

Declaration of Competing Interest

The authors declare that they have no known competing financial interests or personal relationships that could have appeared to influence the work reported in this paper.

Acknowledgment

Yangyang Feng and Chunjia Luo contributed equally to this work. This work was supported by the Shaanxi Key Research and Development Project (2021GY199), National Natural Science Foundation of China (22005039), Public Welfare Science and Technology Projects of Ningbo (2021S150), Natural Science Basic Research Plan in Shaanxi Province of China (2021JQ-224), Shaanxi Key Research and Development Project (2020ZDLGY13-08), Special Fund for Basic Scientific Research of Central Colleges, Chang' an University (300102319306, 300102312403), K. C. Wong Education Foundation (GJTD-2019-13).

Appendix A. Supplementary data

Supplementary data to this article can be found online at https://doi.org/10.1016/j.cej.2022.135910.

References

[1] B. Bruggen, Sustainable implementation of innovative technologies for water purification, Nat. Rev. Chem. 5 (2021) 217–218, https://doi.org/10.1038/s41570-021-00264-7.
[2] W. Yong, H. Zhang, Recent advances in polymer blend membranes for gas separation and pervaporation, Prog. Mater. Sci. 116 (2021), 100713, https://doi.org/10.1016/j.pmatsci.2020.100713.
[3] Q. Lin, G. Zeng, G. Yan, J. Luo, X. Cheng, Z. Zhao, H. Li, Self-cleaning photocatalytic MXene composite membrane for synergistically enhanced water treatment: Oil/water separation and dyes removal, Chem. Eng. J. 427 (2022) 131668.
[4] G. Yang, D. Liu, C. Chen, Y. Qian, Y. Su, S. Qin, L. Zhang, X. Wang, L. Sun, W. Lei, Stable $Ti_3C_2T_x$ MXene-boron nitride membranes with low internal resistance for enhanced salinity gradient energy harvesting, ACS Nano 15 (2021) 6594–6603, https://doi.org/10.1021/acsnano.0c09845.
[5] J. Xia, P. Xiao, J. Gu, T. Chen, C. Liu, L. Yan, T. Chen, Interfacial selfassembled GR/GO ultrathin membranes in large scale for molecular sieving, J. Mater. Chem. A 8 (2020) 18735–18744, https://doi.org/10.1039/D0TA05337F.
[6] Z. Liu, C. Wang, Z. Zhu, Q. Lou, C. Shen, Y. Chen, J. Sun, Y. Ye, J. Zang, L. Dong, C. Shan, Wafer-scale growth of two-dimensional graphitic carbon nitride films, Matter 4 (2021) 1625–1638, https://doi.org/10.1016/j.matt.2021.02.014.
[7] T. Wang, H. Wu, S. Zhao, W. Zhang, M. Tahir, Z. Wang, J. Wang, Interfacial polymerized and pore-variable covalent organic framework composite membrane

for dye separation, Chem. Eng. J. 384 (2020), 123347, https://doi.org/10.1016/j.cej.2019.123347.
[8] B. Sapkota, W. Liang, A. VahidMohammadi, R. Karnik, A. Noy, M. Wanunu, High permeability sub-nanometre sieve composite MoS_2 membranes, Nat. Commun. 11 (2020) 2747, https://doi.org/10.1038/s41467-020-16577-y.
[9] J. Rogacka, A. Seremak, A. Triguero, F. Formalik, I. Martos, L. Firlej, S. Calero, B. Kuchta, High-throughput screening of metal-organic frameworks for CO_2 and CH_4 separation in the presence of water, Chem. Eng. J. 403 (2021), 126392, https://doi.org/10.1016/j.cej.2020.126392.
[10] L. Ding, L. Li, Y. Liu, Y. Wu, Z. Lu, J. Deng, Y. Wei, J. Caro, H. Wang, Effective ion sieving with $Ti_3C_2T_x$ MXene membranes for production of drinking water from seawater, Nat. Sust. 3 (2020) 296–302, https://doi.org/10.1038/s41893-020-0474-0.
[11] J. Wang, Z. Zhang, J. Zhu, M. Tian, S. Zheng, F. Wang, X. Wang, L. Wang, Ion sieving by a two-dimensional $Ti_3C_2T_x$ alginate lamellar membrane with stable interlayer spacing, Nat. Commun. 11 (2020) 3540, https://doi.org/10.1038/s41467-020-17373-4.
[12] Y. Zhao, M. Que, J. Chen, C. Yang, MXenes as co-catalysts for the solar-driven photocatalytic reduction of CO_2, J. Mater. Chem. C 8 (2020) 16258–16281, https://doi.org/10.1039/D0TC02979C.
[13] H. Zheng, J. Chen, M. Que, X. Liu, L. Yang, Y. Zhao, Y. Li, X. Yang, T. Yang, Z. Liu, Light absorption and photocatalytic activity enhanced by in situ formation of uniform TiO_2 nanoparticles on two-dimensional $Ti_3C_2T_x$ surface, J. Alloys Compd. 882 (2021), 160757, https://doi.org/10.1016/j.jallcom.2021.160757.
[14] N. Lu, X. Jing, J. Zhang, P. Zhang, Q. Qiao, Z. Zhang, Photo-assisted self-assembly synthesis of all 2D-layered heterojunction photocatalysts with long-range spatial separation of charge-carriers toward photocatalytic redox reactions, Chem. Eng. J. 431 (2022), 134001, https://doi.org/10.1016/j.cej.2021.134001.
[15] H. Li, J. Li, Z. Ai, F. Jia, L. Zhang, Oxygen vacancy-mediated photocatalysis of BiOCl: Reactivity, selectivity, and perspectives, Angew. Chem. Int. Ed. 57 (2018) 122–138, https://doi.org/10.1002/anie.201705628.
[16] L. Ji, L. Yan, M. Chao, M. Li, J. Gu, M. Lei, Y. Zhang, X. Wang, J. Xia, T. Chen, Y. Nie, T. Chen, Sphagnum inspired g-C_3N_4 nano/microspheres with smaller bandgap in heterojunction membranes for sunlight-driven water purification, Small 17 (2021) 2007122, https://doi.org/10.1002/smll.202007122.
[17] N. Li, Z. Xu, S. Zheng, H. Dai, L. Wang, Y. Tian, Z. Dong, L. Jiang, Superamphiphilic TiO_2 composite surface for protein antifouling, Adv. Mater. 33 (2021) 2003559, https://doi.org/10.1002/adma.202003559.
[18] J. Hu, Y. Zhan, G. Zhang, Q. Feng, W. Yang, Y. Chiao, S. Zhang, A. Sun, Durable and super-hydrophilic/underwater super-oleophobic two-dimensional MXene composite lamellar membrane with photocatalytic self-cleaning property for efficient oil/water separation in harsh environments, J. Membr. Sci. 637 (2021), 119627, https://doi.org/10.1016/j.memsci.2021.119627.
[19] Z. Huang, Q. Zeng, Y. Liu, Y. Xu, R. Li, H. Hong, L. Shen, H. Lin, Facile synthesis of 2D TiO_2@MXene composite membrane with enhanced separation and antifouling performance, J. Membr. Sci. 640 (2021), 119854, https://doi.org/10.1016/j.memsci.2021.119854.
[20] K. Yoon, K. Lee, S. Jo, S. Yook, K. Lee, I. Kim, J. Kim, Mussel-inspired polydopamine-treated reinforced composite membranes with self-supported CeOx radical scavengers for highly stable PEM fuel cells, Adv. Funct. Mater. 29 (2019) 1806929, https://doi.org/10.1002/adfm.201806929.
[21] Y. Fang, Z. Liu, J. Han, Z. Jin, Y. Han, F. Wang, Y. Niu, Y. Wu, Y. Xu, High-performance electrocatalytic conversion of N_2 to NH_3 using oxygen-vacancy-rich TiO_2 in situ grown on $Ti_3C_2T_x$ MXene, Adv. Energy Mater. 9 (2019) 1803406, https://doi.org/10.1002/aenm.201803406.
[22] Y. Xiao, G. Tian, W. Li, Y. Xie, B. Jiang, C. Tian, D. Zhao, H. Fu, Molecule self-assembly synthesis of porous few-layer carbon nitride for highly efficient photoredox catalysis, J. Am. Chem. Soc. 141 (2019) 2508–2515, https://doi.org/10.1021/jacs.8b12428.
[23] C. Yang, Q. Tan, Q. Li, J. Zhou, J. Fan, B. Li, J. Sun, K. Lv, 2D/2D Ti_3C_2 MXene/g-C_3N_4 nanosheets heterojunction for high efficient CO_2 reduction photocatalyst: Dual effects of urea, Appl. Catal. B Environ. 268 (2020), 118738, https://doi.org/10.1016/j.apcatb.2020.118738.
[24] Z. Lu, Y. Wei, J. Deng, L. Ding, Z. Li, H. Wang, Self-crosslinked MXene ($Ti_3C_2T_x$) membranes with good antiswelling property for monovalent metal ion exclusion, ACS Nano 13 (2019) 10535–10544, https://doi.org/10.1021/acsnano.9b04612.
[25] Z. Li, Y. Wei, X. Gao, L. Ding, Z. Lu, J. Deng, X. Yang, J. Caro, H. Wang, Antibiotics separation with MXene membranes based on regularly stacked high-aspect-ratio nanosheets, Angew. Chem. Int. Ed. 59 (2020) 9751–9756, https://doi.org/10.1002/anie.202002935.
[26] K. Huang, C. Li, X. Meng, In-situ construction of ternary Ti_3C_2 MXene@TiO_2/$ZnIn_2S_4$ composites for highly efficient photocatalytic hydrogen evolution, J. Colloid Interface Sci. 580 (2020) 669–680, https://doi.org/10.1016/j.jcis.2020.07.044.
[27] J. Wang, Y. Shen, S. Liu, Y. Zhang, Single 2D MXene precursor-derived TiO_2 nanosheets with a uniform decoration of amorphous carbon for enhancing photocatalytic water splitting, Appl. Catal. B Environ. 270 (2020), 118885, https://doi.org/10.1016/j.apcatb.2020.118885.
[28] F. Xia, J. Lao, R. Yu, X. Sang, J. Luo, Y. Li, J. Wu, Ambient oxidation of Ti_3C_2 MXene initialized by atomic defects, Nanoscale 11 (2019) 23330–23337, https://doi.org/10.1039/C9NR07236E.
[29] S. Wei, S. Ni, X. Xu, A new approach to inducing Ti^{3+} in anatase TiO_2 for efficient photocatalytic hydrogen production, Chin. J. Catal. 39 (2018) 510–516, https://doi.org/10.1016/S1872-2067(17)62968-1.
[30] J. Zhou, M. Xie, F. Wu, Y. Mei, Y. Hao, L. Li, R. Chen, Encapsulation of metallic Zn in a hybrid MXene/graphene aerogel as a stable Zn anode for foldable Zn-Ion batteries, Adv. Mater. 34 (2022) 2106897, https://doi.org/10.1002/adma.202106897.
[31] Q. Xu, W. Yang, Y. Wen, S. Liu, Z. Liu, W. Ong, N. Li, Hydrochromic full-color MXene quantum dots through hydrogen bonding toward ultrahigh-efficiency white light-emitting diodes, Appl. Mater. Today 16 (2019) 90–101, https://doi.org/10.1016/j.apmt.2019.05.001.
[32] S. Wan, X. Li, Y. Wang, Y. Chen, X. Xie, R. Yang, A. Tomsia, L. Jiang, Q. Cheng, Strong sequentially bridged MXene sheets, PNAS 117 (2020) 27154–27161, https://doi.org/10.1073/pnas.2009432117.
[33] T. Liu, X. Liu, N. Graham, W. Yu, K. Sun, Two-dimensional MXene incorporated graphene oxide composite membrane with enhanced water purification performance, J. Membr. Sci. 593 (2020), 117431, https://doi.org/10.1016/j.memsci.2019.117431.
[34] H. Huang, Y. Song, N. Li, D. Chen, Q. Xu, H. Li, J. He, J. Lu, One-step in-situ preparation of N-doped TiO_2@C derived from Ti_3C_2 MXene for enhanced visible-light driven photodegradation, Appl. Catal. B Environ. 251 (2019) 154–161, https://doi.org/10.1016/j.apcatb.2019.03.066.
[35] S. He, Y. Zhan, J. Hu, G. Zhang, S. Zhao, Q. Feng, W. Yang, Chemically stable two-dimensional MXene@UIO-66-$(COOH)_2$ composite lamellar membrane for multi-component pollutant-oil-water emulsion separation, Compos. Part B Eng. 197 (2020), 108188, https://doi.org/10.1016/j.compositesb.2020.108188.
[36] F. Li, D. Benetti, M. Zhang, J. Feng, Q. Wei, F. Rosei, Modulating the 0D/2D interface of hybrid semiconductors for enhanced photoelectrochemical performances, Small Methods 5 (2021) 2100109, https://doi.org/10.1002/smtd.202100109.
[37] G. Li, N. Li, S. Peng, B. He, J. Wang, Y. Du, W. Zhang, K. Han, F. Dang, Highly efficient Nb_2C MXene cathode catalyst with uniform O-terminated surface for lithium–oxygen batteries, Adv. Energy Mater. 11 (2021) 2002721, https://doi.org/10.1002/aenm.202002721.
[38] Z. Li, Y. Liu, L. Li, Y. Wei, J. Caro, H. Wang, Ultra-thin titanium carbide (MXene) sheet membranes for high-efficient oil/water emulsions separation, J. Membr. Sci. 592 (2019), 117361, https://doi.org/10.1016/j.memsci.2019.117361.
[39] J. He, P. Wu, L. Chen, H. Li, M. Hua, L. Lu, Y. Wei, Y. Chao, S. Zhou, W. Zhu, H. Li, Dynamically-generated TiO_2 active site on MXene Ti_3C_2: Boosting reactive desulfurization, Chem. Eng. J. 416 (2021), 129022, https://doi.org/10.1016/j.cej.2021.129022.
[40] F. He, B. Zhu, B. Cheng, J. Yu, W. Ho, W. Macyk, 2D/2D/0D TiO_2/C_3N_4/Ti_3C_2 MXene composite S-scheme photocatalyst with enhanced CO_2 reduction activity, Appl. Catal. B Environ. 272 (2020), 119006, https://doi.org/10.1016/j.apcatb.2020.119006.
[41] N. Liu, N. Lu, Y. Su, P. Wang, X. Quan, Fabrication of g-C_3N_4/Ti_3C_2 composite and its visible-light photocatalytic capability for ciprofloxacin degradation, Sep. Purif. Technol. 211 (2019) 782–789, https://doi.org/10.1016/j.seppur.2018.10.027.
[42] Y. Cai, D. Chen, N. Li, Q. Xu, H. Li, J. He, J. Lu, A self-cleaning heterostructured membrane for efficient oil-in-water emulsion separation with stable flux, Adv. Mater. 32 (2020) 2001265, https://doi.org/10.1002/adma.202001265.
[43] B. Liang, G. Zhang, Z. Zhong, T. Sato, A. Hozumi, Z. Su, Substrate-independent polyzwitterionic coating for oil/water separation membranes, Chem. Eng. J. 362 (2019) 126–135, https://doi.org/10.1016/j.cej.2019.01.013.
[44] J. Qian, S. Zhao, W. Dang, Y. Liao, W. Zhang, H. Wang, L. Lv, L. Luo, H. Jiang, J. Tang, Photocatalytic nitrogen reduction by Ti_3C_2 MXene derived oxygen vacancy-rich C/TiO_2, Adv. Sustainable Syst. 5 (2021) 2000282, https://doi.org/10.1002/adsu.202000282.
[45] K. Xiang, D. Wu, Y. Fan, W. You, D. Zhang, J. Luo, X. Fu, Enhancing bifunctional electrodes of oxygen vacancy abundant $ZnCo_2O_4$ nanosheets for supercapacitor and oxygen evolution, Chem. Eng. J. 425 (2021), 130583, https://doi.org/10.1016/j.cej.2021.130583.
[46] S. Zhang, Z. Liu, D. Chen, Z. Guo, M. Ruan, Oxygen vacancies engineering in TiO_2 homojunction/ZnFe-LDH for enhanced photoelectrochemical water oxidation, Chem. Eng. J. 395 (2020), 125101, https://doi.org/10.1016/j.cej.2020.125101.
[47] C. Liu, W. Wang, M. Zhang, C. Zhang, C. Ma, L. Cao, D. Kong, H. Feng, W. Li, S. Chen, Synthesis of MXene/COF/Cu_2O heterojunction for photocatalytic bactericidal activity and mechanism evaluation, Chem. Eng. J. 430 (2022), 132663, https://doi.org/10.1016/j.cej.2021.132663.
[48] M. Naguib, V. Mochalin, M. Barsoum, Y. Gogotsi, 25th anniversary article: MXenes: A new family of two-dimensional materials, Adv. Mater. 26 (2014) 992–1005, https://doi.org/10.1002/adma.201304138.
[49] L. Wang, G. Tang, S. Liu, H. Dong, Q. Liu, J. Sun, H. Tang, Interfacial active-site-rich 0D Co_3O_4/1D TiO_2 p-n heterojunction for enhanced photocatalytic hydrogen evolution, Chem. Eng. J. 428 (2022), 131338, https://doi.org/10.1016/j.cej.2021.131338.
[50] X. Han, L. An, Y. Hu, Y. Li, C. Hou, H. Wang, Q. Zhang, Ti_3C_2 MXene-derived carbon-doped TiO_2 coupled with g-C_3N_4 as the visible-light photocatalysts for photocatalytic H_2 generation, Appl. Catal. B Environ. 265 (2020), 118539, https://doi.org/10.1016/j.apcatb.2019.118539.
[51] H. Shi, S. Long, S. Hu, J. Hou, W. Ni, C. Song, K. Li, G. Gurzadyan, X. Guo, Interfacial charge transfer in 0D/2D defect-rich heterostructures for efficient solar-driven CO_2 reduction, Appl. Catal. B Environ. 245 (2019) 760–769, https://doi.org/10.1016/j.apcatb.2019.01.036.
[52] H. Zhu, Q. Xue, G. Zhu, Y. Liu, X. Dou, X. Yuan, Decorating Pt@cyclodextrin nanoclusters on C_3N_4/MXene for boosting the photocatalytic H_2O_2 production, J. Mater. Chem. A 9 (2021) 6872–6880, https://doi.org/10.1039/D0TA10742E.
[53] B. Li, H. Song, F. Han, L. Wei, Photocatalytic oxidative desulfurization and denitrogenation for fuels in ambient air over Ti_3C_2/g-C_3N_4 composites under visible light irradiation, Appl. Catal. B Environ. 269 (2020), 118845, https://doi.org/10.1016/j.apcatb.2020.118845.

[54] Q. Liu, L. Ai, J. Jiang, MXene-derived TiO_2@C/g-C_3N_4 heterojunctions for highly efficient nitrogen photofixation, J. Mater. Chem. A 6 (2018) 4102–4110, https://doi.org/10.1039/C7TA09350K.
[55] S. Lu, G. Meng, C. Wang, H. Chen, Photocatalytic inactivation of airborne bacteria in a polyurethane foam reactor loaded with a hybrid of MXene and anatase TiO2 exposing 0 0 1 facets, Chem. Eng. J. 404 (2021), 126526, https://doi.org/10.1016/j.cej.2020.126526.
[56] S. Luan, D. Qu, L. An, W. Jiang, X. Gao, S. Hua, X. Miao, Y. Wen, Z. Sun, Enhancing photocatalytic performance by constructing ultrafine TiO_2 nanorods/g-C_3N_4 nanosheets heterojunction for water treatment, Sci. Bull. 63 (2018) 683–690, https://doi.org/10.1016/j.scib.2018.04.002.
[57] W. Wang, X. Bai, Q. Ci, L. Du, X. Ren, D. Phillips, Near-field drives long-lived shallow trapping of polymeric C_3N_4 for efficient photocatalytic hydrogen evolution, Adv. Funct. Mater. 31 (2021) 2103978, https://doi.org/10.1002/adfm.202103978.
[58] Y. Zou, B. Yang, Y. Liu, Y. Ren, J. Ma, X. Zhou, X. Cheng, Y. Deng, Controllable interface-induced co-assembly toward highly ordered mesoporous Pt@TiO_2/g-C_3N_4 heterojunctions with enhanced photocatalytic performance, Adv. Funct. Mater. 28 (2018) 1806214, https://doi.org/10.1002/adfm.201806214.
[59] Z. Wang, Z. Wang, X. Zhu, C. Ai, Y. Zeng, W. Shi, X. Zhang, H. Zhang, H. Si, J. Li, C. Wang, S. Lin, Photodepositing CdS on the active cyano groups decorated g-C_3N_4 in Z-scheme manner promotes visible-light-driven hydrogen evolution, Small 17 (2021) 2102699, https://doi.org/10.1002/smll.202102699.
[60] L. Tie, S. Yang, C. Yu, H. Chen, Y. Liu, S. Dong, J. Sun, J. Sun, In situ decoration of ZnS nanoparticles with Ti_3C_2 MXene nanosheets for efficient photocatalytic hydrogen evolution, J. Colloid Interface Sci. 545 (2019) 63–70, https://doi.org/10.1016/j.jcis.2019.03.014.
[61] Y. Li, M. Gu, T. Shi, W. Cui, X. Zhang, F. Dong, J. Cheng, J. Fan, K. Lv, Carbon vacancy in C_3N_4 nanotube: Electronic structure, photocatalysis mechanism and highly enhanced activity, Appl. Catal. B Environ. 262 (2020), 118281, https://doi.org/10.1016/j.apcatb.2019.118281.
[62] C. Feng, L. Tang, Y. Deng, J. Wang, J. Luo, Y. Liu, X. Ouyang, H. Yang, J. Yu, J. Wang, Synthesis of leaf-vein-like g-C_3N_4 with tunable band structures and charge transfer properties for selective photocatalytic H_2O_2 evolution, Adv. Funct. Mater. 30 (2020) 2001922, https://doi.org/10.1002/adfm.202001922.
[63] K. Wu, S. Song, H. Wu, J. Guo, L. Zhang, Facile synthesis of Bi_2WO_6/C_3N_4/Ti_3C_2 composite as Z-scheme photocatalyst for efficient ciprofloxacin degradation and H_2 production, Appl. Catal. A Gen. 608 (2020), 117869, https://doi.org/10.1016/j.apcata.2020.117869.
[64] H. Zheng, X. Meng, J. Chen, M. Que, W. Wang, X. Liu, L. Yang, Y. Zhao, In situ phase evolution of TiO_2/$Ti_3C_2T_x$ heterojunction for enhancing adsorption and photocatalytic degradation, Appl. Surf. Sci. 545 (2021), 149031, https://doi.org/10.1016/j.apsusc.2021.149031.
[65] L. Yang, J. Chen, X. Liu, M. Que, Y. Zhao, H. Zheng, T. Yang, Z. Liu, Y. Li, X. Yang, 2D/2D BiOBr/(001)-TiO_2 heterojunction toward enhanced photocatalytic degradation activity of Rhodamine B, J. Alloys Compd. 884 (2021), 161064, https://doi.org/10.1016/j.jallcom.2021.161064.
[66] J. Li, Y. Sun, L. Zhang, X. Xiao, N. Yang, L. Zhang, X. Yang, F. Peng, B. Jiang, Visible-light induced $CoMoO_4$@Bi_2MoO_6 heterojunction membrane with attractive photocatalytic property and high precision separation toward oil-in-water emulsion, Sep. Purif. Technol. 277 (2021), 119568, https://doi.org/10.1016/j.seppur.2021.119568.
[67] C. Liu, J. Xia, J. Gu, W. Wang, Q. Liu, L. Yan, T. Chen, Multifunctional CNTs-PAA/MIL101(Fe)@Pt composite membrane for high-throughput oily wastewater remediation, J. Hazard. Mater. 403 (2021), 123547, https://doi.org/10.1016/j.jhazmat.2020.123547.
[68] L. Chen, X. Xie, X. Song, S. Luo, S. Ye, W. Situ, Photocatalytic degradation of ethylene in cold storage using the nanocomposite photocatalyst MIL101(Fe)-TiO_2-rGO, Chem. Eng. J. 424 (2021), 130407, https://doi.org/10.1016/j.cej.2021.130407.
[69] C. Lops, A. Ancona, K. Cesare, B. Dumontel, N. Garino, G. Canavese, S. Hérnandez, V. Cauda, Sonophotocatalytic degradation mechanisms of Rhodamine B dye via radicals generation by micro- and nano-particles of ZnO, Appl. Catal. B Environ. 243 (2019) 629–640, https://doi.org/10.1016/j.apcatb.2018.10.078.
[70] Z. Liu, Y. Liu, X. Sun, H. Ji, W. Liu, Z. Cai, Construction of Z-scheme Ag/$AgVO_3$/carbon-rich g-C_3N_4 heterojunction for enhanced photocatalytic degradation of sulfamethiadiazole: DFT calculation and mechanism study, Chem. Eng. J. 433 (2022) 133604.
[71] Y. Zhang, P. Chen, Q. Wang, Q. Wang, K. Zhu, K. Ye, G. Wang, D. Cao, J. Yan, Q. Zhang, High-capacity and kinetically accelerated lithium storage in MoO_3 enabled by oxygen vacancies and heterostructure, Adv. Energy Mater. 11 (2021) 2101712, https://doi.org/10.1002/aenm.202101712.